# Absolute local conformation of poly(methyl methacrylate) chains adsorbed on a quartz surface

Kawaguchi, Daisuke
Department of Applied Chemistry, Kyushu University

Sasahara, Kazuki
Department of Applied Chemistry, Kyushu University

Inutsuka, Manabu
Department of Applied Chemistry, Kyushu University

Abe, Tatsuki
Department of Applied Chemistry, Kyushu University

他



出版情報：The journal of chemical physics. 159 (24), pp.244902-1-244902-8, 2023-12-26. AIP Publishing
バージョン：

The Journal of Chemical Physics

RESEARCH ARTICLE | DECEMBER 26 2023

# Absolute local conformation of poly(methyl methacrylate) chains adsorbed on a quartz surface

**Special Collection:** Polymer Nanoconfinement

Daisuke Kawaguchi ; Kazuki Sasahara; Manabu Inutsuka; Tatsuki Abe ; Satoru Yamamoto ; Keiji Tanaka



*J. Chem. Phys.* 159, 244902 (2023)
https://doi.org/10.1063/5.0184315
CHORUS

The Journal of Chemical Physics ARTICLE pubs.aip.org/aip/jcp

# Absolute local conformation of poly(methyl methacrylate) chains adsorbed on a quartz surface

Cite as: J. Chem. Phys. 159, 244902 (2023); doi: 10.1063/5.0184315
Submitted: 25 October 2023 • Accepted: 30 November 2023 •
Published Online: 26 December 2023



Daisuke Kawaguchi,[1,2,a),b)] Kazuki Sasahara,[1] Manabu Inutsuka,[1,c)] Tatsuki Abe,[1] Satoru Yamamoto,[2] and Keiji Tanaka[1,2,a)]

## AFFILIATIONS

[1] Department of Applied Chemistry, Kyushu University, Fukuoka 819-0395, Japan
[2] Center for Polymer Interface and Molecular Adhesion Science, Kyushu University, Fukuoka 819-0395, Japan

**Note:** This paper is part of the JCP Special Topic on Polymer Nanoconfinement.
[a)] **Authors to whom correspondence should be addressed:** kawaguchi@chembio.t.u-tokyo.ac.jp and k-tanaka@cstf.kyushu-u.ac.jp
[b)] **Present address:** Department of Chemistry and Biotechnology, Graduate School of Engineering, The University of Tokyo, Tokyo 113-8656, Japan.
[c)] **Present address:** Waseda Center for a Carbon Neutral Society, Waseda University, Tokyo 169-8555, Japan.

## ABSTRACT

Polymer chains at a buried interface with an inorganic solid play a critical role in the performance of polymer nanocomposites and adhesives. Sum frequency generation (SFG) vibrational spectroscopy with a sub-nanometer depth resolution provides valuable information regarding the orientation angle of functional groups at interfaces. However, in the case of conventional SFG, since the signal intensity is proportional to the square of the second-order nonlinear optical susceptibility and thereby loses phase information, it cannot be unambiguously determined whether the functional groups face upward or downward. This problem can be solved by phase-sensitive SFG (ps-SFG). We here applied ps-SFG to poly(methyl methacrylate) (PMMA) chains in direct contact with a quartz surface, shedding light on the local conformation of chains adsorbed onto the solid surface. The measurements made it possible to determine the absolute orientation of the ester methyl groups of PMMA, which were oriented toward the quartz interface. Combining ps-SFG with all-atomistic molecular dynamics simulation, the distribution of the local conformation and the driving force are also discussed.





## INTRODUCTION

Polymer/inorganic solid interfaces are ubiquitous and can be found in various materials such as polymer nanocomposites,[1–11] thin-film devices,[12–18] and adhesives.[19–24] When chains come into contact with a solid surface, they are subjected to adsorption if the enthalpic gain from the interaction between segments and the solid surface outweighs the entropic penalty due to the restricted conformation. Previous studies have shown that when a composite material, composed of a rubbery polymer and a carbon black filler, is washed with a good solvent, a polymer layer with two types of adsorbed chains remains on the filler.[25–27] Similarly, when a polymer film supported on a solid substrate is well annealed, an adsorbed layer is formed on the solid surface.[28–33] The dynamics of chains in the interfacial layer are markedly different from those of the corresponding bulk chains.[34–44] These characteristics of chains in the interfacial layer are universal for rubbery and glassy polymers,[45–49] as mentioned earlier, and are closely related to the mechanical properties of the polymer nanocomposites.[50–55]

A general model for a chain adsorbed onto a solid surface, known as the loop-train-tail model,[56,57] has been proposed. In this model, the loop and train conformations consist of segments in direct contact with the solid surface and segments away from the surface, respectively. Atomic force microscopy observations have suggested that loop segments transform into train ones if molecular motion on a relatively large scale is allowed.[58] In addition,

discussions have centered on how the interfacial layer forms from individual chains.[59] These observations lend support to the hypothesis that the enthalpic gain from the interaction between segments and the solid surface outweighs the penalty of conformational entropy. However, there appears to be limited direct evidence regarding the interaction between segments and the substrate.

Sum frequency generation (SFG) vibrational spectroscopy enables us to gain access to information about functional groups at interfaces with a molecular-level resolution along the depth direction.[60,61] We have hitherto applied SFG to detect changes in the local conformation of functional groups at various interfaces when exposed to changing environmental conditions, including temperature, allowing for discussions on the molecular motion of polymers at these interfaces.[62–70] However, conventional SFG, in which the signal intensity is proportional to the square of the second-order nonlinear optical susceptibility ($\chi_{\mathrm{eff}}^{(2)}$), suffers from the loss of phase information. This makes it challenging to unambiguously determine whether the functional groups are oriented upward or downward, hindering a direct analysis of the interaction between segments and the solid surface. On the other hand, phase-sensitive (ps) SFG measurements directly provide the imaginary part of $\chi_{\mathrm{eff}}^{(2)}$ (Im $\chi_{\mathrm{eff}}^{(2)}$), which is analogous to the imaginary part of the linear dielectric constant ($\varepsilon$) in linear absorption spectroscopy.[71–74] The Im $\chi_{\mathrm{eff}}^{(2)}$ determines the orientation of moieties contributing to the resonance.[74,75] Therefore, ps-SFG measurements have the potential to elucidate the adsorption process of chains in direct contact with an inorganic solid. The ps-SFG measurements have been applied to various interfaces,[76–81] but the number of reports applying them to polymer systems,[82–85] particularly on a buried solid interface,[86] remains limited owing to the difficulty of obtaining sufficient SFG signal intensity.

The objective of this study is to experimentally elucidate the absolute local conformation of chains that are in direct contact with a solid surface buried within a material. To achieve this, we used ps-SFG measurements on a model system, poly(methyl methacrylate) (PMMA), in direct contact with a quartz surface. The obtained results are then discussed in conjunction with all atomistic molecular dynamics (MD) simulations. This information enhances our understanding of the aggregation states and dynamics of polymer chains in nanoconfinement. Such insights are crucial for the development of nanocomposites and thin-film devices.

## EXPERIMENTAL

### Materials and sample preparation

PMMA purchased from Polymer Source, Inc. (Dorval, QC, Canada) was used. The number-average molecular weight ($M_n$) and polydispersity index ($M_w/M_n$) were 15k and 1.15, respectively, where $M_w$ represented the weight-average molecular weight. The bulk glass transition temperature ($T_g^b$) of PMMA was determined to be 398 K using differential scanning calorimetry (DSC6220, SII Nanotechnologys Inc., Tokyo, Japan). For both conventional and ps-SFG measurements, a half-cylindrical fused quartz prism and a fused quartz window were used as common substrates. Additionally, a z-cut quartz window was used as a substrate specifically for ps-SFG measurements. This choice was made because it had a surface chemistry similar to fused quartz and exhibited the ability to generate SFG signals. Prior to use, the substrates were immersed in a piranha solution [$H_2SO_4$:$H_2O_2$ = 8:2 (v/v)] at 373 K for 2 h and then thoroughly washed with distilled water. Panel (a) of Fig. 1 depicts the sample configuration used for both conventional and ps-SFG measurements. First, PMMA films were prepared by a solvent-casting method from its toluene solution onto three types of substrates: fused quartz prism, fused quartz window, and z-cut quartz window. Subsequently, two films were attached together in a face-to-face configuration and dried under vacuum at room temperature for 24 h, which was below the $T_g^b$. This means that the sample was initially in a non-equilibrium state. For the conventional SFG measurement, the film sandwiched between the fused quartz prism and window was used. On the other hand, for the ps-SFG measurement, the film sandwiched between the z-cut quartz window and the fused quartz window was used. The thickness of the sandwiched films was between 1 and 44 $\mu$m, as measured by a micrometer. The use of thick films was intended to capture SFG signals exclusively from the upper interface. The details are discussed in the later part.

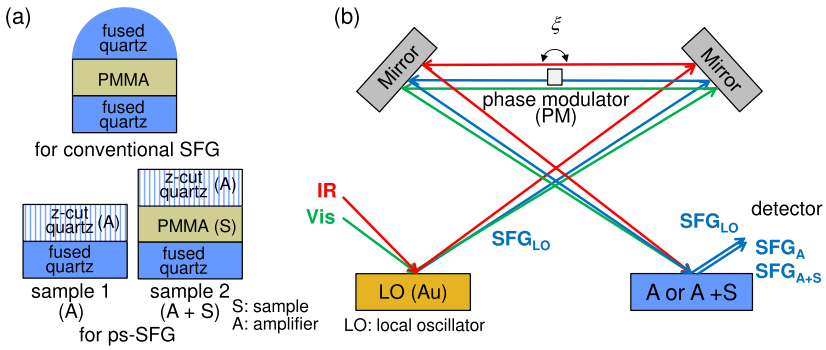


**FIG. 1.** Schematic illustration of (a) sample configuration for conventional and ps-SFG measurements and (b) optical configuration for ps-SFG measurements. PMMA and z-cut quartz are the polymer sample and an amplifier for SFG signals, respectively.

### Conventional SFG

The conformational change in polymer chains at the quartz interface was examined before and after thermal annealing by conventional SFG measurements. The visible beam with a wavelength of 532 nm was generated by frequency-doubling fundamental output pulses from a picosecond Nd:YAG laser (PL2231-50-FT, EKSPLA, Vilnius, Lithuania). The tunable infrared (IR) beam was generated from an EKSPLA optical parametric generation/amplification and difference frequency generation (OPG/OPA/DFG) system based on lithium triborate (LBO) and $AgGaS_2$ crystals. The incident angles of the visible and IR beams were 65° and 55°, respectively. All measurements were conducted at room temperature. An as-dried sample was first measured and then remeasured at room temperature after being annealed at 433 K for 24 h under vacuum.

### ps-SFG

The absolute orientation of the local conformation for PMMA at the quartz interface was examined by ps-SFG measurements. Figure 1(b) provides an illustration of the optical configuration used in the measurements. The excited visible and IR beams were identical to those used in the conventional one. The input visible and IR beams were focused onto a local oscillator (LO) consisting of an Au mirror (THORLABS, Inc.) to generate an SFG signal ($SFG_{LO}$). This $SFG_{LO}$ signal was then directed into the sample through a phase modulator (PM) made of fused quartz. Simultaneously, the input visible and IR beams, reflected from the LO and mirrors, were once again focused onto the sample to generate an SFG signal ($SFG_S$). However, a technical challenge arose due to the markedly lower intensity of $SFG_S$ signals at the buried interface, resulting in a poor interferogram. To overcome this, a z-cut quartz window was used as an amplifier of the SFG signals and also served as a substrate. A stack comprising fused quartz and z-cut quartz windows, named sample 1, was used as a reference. Additionally, the PMMA film sandwiched between the z-cut and fused quartz windows was labeled as sample 2. Z-cut quartz and PMMA, which serve as amplifiers for SFG signals and a polymer sample of interest, will be subsequently abbreviated as A and S, respectively. The SFG signals obtained from samples 1 and 2 were referred to as $SFG_A$ and $SFG_{A+S}$, respectively. The interfered signals from samples 1 and 2 were detected as a function of the wavenumber of the input IR beam using a photomultiplier. The extent of the interference was altered by rotating the PM. Finally, the interferograms from A and S + A were obtained.

The phase information at the PMMA/quartz interface was extracted from the interferograms obtained from A and S + A. Details of how to extract the phase information are provided in the supplementary material. The effective second-order nonlinear susceptibility ($\chi_{eff}^{(2)}$) of a functional group was determined by using the phase of the SFG signals from S ($\phi_S$). Since the magnitude of $|\chi_{eff}^{(2)}|$ is proportional to the square root of the SFG intensity, the real and imaginary parts of $\chi_{eff}^{(2)}$ can be expressed as follows:

$$\mathrm{Re}\,\chi_{eff}^{(2)} + i\,\mathrm{Im}\,\chi_{eff}^{(2)} = \left|\chi_{eff}^{(2)}\right| \cos\,\phi_S + i\left|\chi_{eff}^{(2)}\right| \sin\,\phi_S. \quad (1)$$

The ps-SFG measurements were conducted at room temperature under the polarization combination of *ssp* (SFG/*s*, visible/*s*, and IR/*p*).

### MD simulation

Molecular dynamics (MD) simulations were conducted using Materials Studio 2021 (Dassault Systèmes, Vélizy-Villacoublay, France) to examine the detailed atomistic structure of PMMA at the quartz interface. The simulation model was prepared using the following steps. A repeating unit of $SiO_2$ was cleaved along the (001) crystallographic orientation, and unsaturated oxygen atoms at the surface were capped with hydrogen atoms, resulting in a surface with Si–OH groups. The density of PMMA in the model was 1.023 g $cm^{-3}$, which was determined through an MD simulation using an NPT ensemble at 298 K in the bulk system. Five PMMA (*rr* triads: 100%) chains with a molecular weight of 15k were packed into a cell while maintaining a constant density. Finally, the cell containing the PMMA chains was placed on the quartz surface to produce the initial model. The lattice size was 8 nm along the *z* axis and 5 nm along the *x* and *y* axes. In the simulation, the position of one Si–O layer located at the center of the quartz surface was fixed in Cartesian coordinates to restrict translational motion along the *z*-axis. The distance between the edge of PMMA and the fixed $SiO_2$ layer was greater than the cutoff distance, ensuring it did not affect the results. Prior to starting the simulation, the system underwent equilibration through the following two steps. Segmental relaxation was performed at 700 K for 500 ps, which was considered sufficient based on the Vogel–Fulcher–Tammann (VFT) equation.[87] The system was then aged at 298 K for 1 ns. These MD simulations were conducted using the Forcite module with the COMPASS III force field. The integration step was set to 1.0 fs, and a Berendsen loose-coupling thermostat was used for temperature control. Van der Waals interactions were calculated using an atom-based method, while electrostatic interactions were handled using the Ewald method. The cutoff distance for van der Waals interactions was set to 1.25 nm.[88] The simulations were performed for six different initial conditions individually. The steady-state information was analyzed from the latter 500 ps of a 1 ns simulation. It was confirmed that the analysis results from this calculation were consistent with those obtained from a 10 ns calculation at 298 K. The above-mentioned MD simulation was conducted using three different initial states, and the statistical data were obtained from them.

## RESULTS AND DISCUSSION

The conformational change of PMMA at the quartz interface before and after annealing was examined by conventional SFG measurements. Figure 2 shows conventional SFG spectra for a PMMA film sandwiched between a fused quartz prism and window under the *ssp* condition. The spectra were normalized by the maximum intensity of each spectrum and vertically shifted for the sake of clarity. Peaks at 2908 and 2936 $cm^{-1}$ were identified as the symmetric and anti-symmetric C–H stretching modes of methylene groups ($CH_2$s and $CH_2$as).[89,90] In addition, a peak at 2950 $cm^{-1}$ could be assigned to the symmetric C–H stretching mode of ester methyl groups ($OCH_3$s).[64,89,90]

The trend of the orientational change in $CH_2$ and $OCH_3$ groups induced by thermal annealing is considered. The intensity of the SFG signals from functional groups is generally influenced by both the orientation and population of those groups. The tilt angle of a $CH_2$

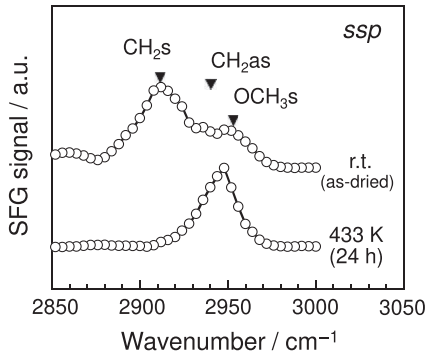


**FIG. 2.** Conventional SFG spectra for a PMMA film sandwiched between quartz before and after annealing at 433 K for 24 h.

group ($\theta_{CH_2}$) was defined as the angle between the interface normal (z-axis) and the direction along the bisector line of the two C–H bonds, which corresponds to the *c*-axis in the molecular coordinate system.[89,91] On the other hand, the tilt angle of an $OCH_3$ group ($\theta_{OCH_3}$) was defined as the angle between the interface normal and the O–C bond vector of the $OCH_3$ group, which also corresponds to the *c*-axis.[89,91] The *ssp* polarization combination enables us to obtain information about the orientation of functional groups along the direction normal to the interface. As $\theta_{CH_2}$ and $\theta_{OCH_3}$ approach 0°, indicating a more aligned orientation of $CH_2$ and $OCH_3$ groups with respect to the interface normal, the *ssp* SFG intensity of those groups tends to increase.

In the case of the as-dried film, the peak intensity from $CH_2$s was relatively higher than that from $CH_2$as and $OCH_3$s. This implies that $CH_2$ groups were oriented toward the interface, while $OCH_3$ groups were less oriented than $CH_2$ groups. However, following the annealing of the film, SFG signals from $CH_2$s disappeared, and those from $CH_2$as became more pronounced. In addition, the signals from $OCH_3$s increased. The shape of the SFG spectrum became consistent with that of well-annealed PMMA films.[64,89] These observed spectral changes indicate that $CH_2$ groups became less oriented and/or inclined toward the interface due to the annealing treatment. Additionally, $OCH_3$ groups became more oriented, aligning themselves in the direction normal to the interface. For quantitative analysis, $\theta_{OCH_3}$ was estimated from the peak intensity ratio of $OCH_3$s obtained under the *ssp* and *ppp* conditions ($I_{ssp}/I_{ppp}$), as explained in the supplementary material. The $\theta_{OCH_3}$ value obtained under the assumption of no angular distribution was 63°. This value will be compared with the MD simulation results later on.

The ps-SFG measurements were performed to examine the absolute orientation of functional groups. Panel (a) of Fig. 3 shows an interferogram for sample 1 in the wavenumber range from 2900 to 3000 $cm^{-1}$, where $CH_2$s, $CH_2$as, and $OCH_3$s peaks appear. It

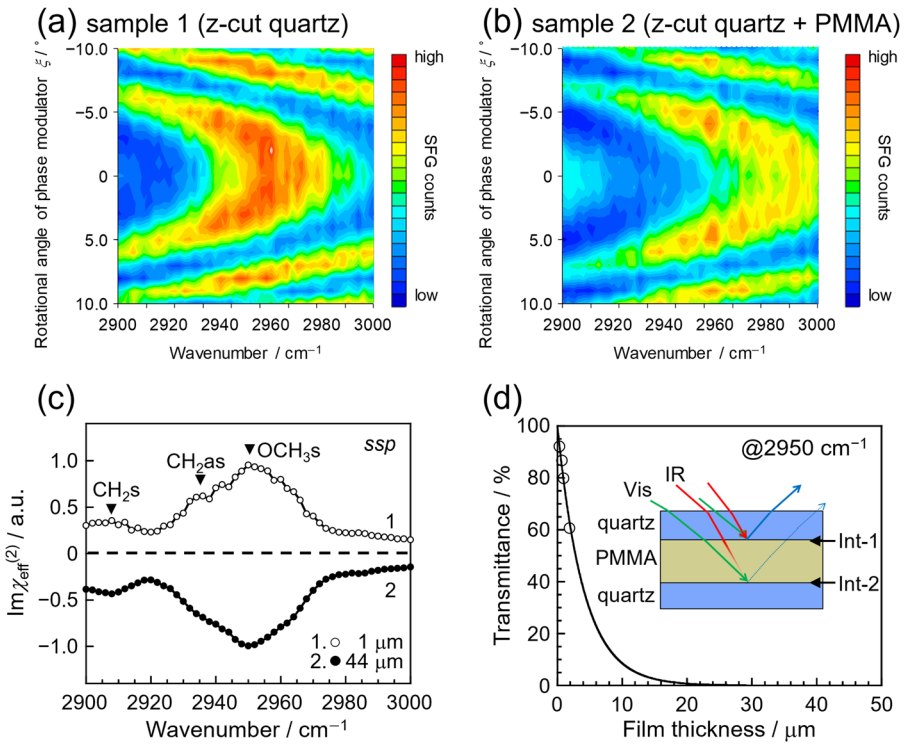


**FIG. 3.** Interferograms for (a) a z-cut quartz window and (b) a PMMA film sandwiched between z-cut and fused quartz windows. (c) Im $\chi_{eff}^{(2)}$ spectra in the C–H stretching vibrational region with a polarization combination of *ssp* for 1 and 44 $\mu$m-thick PMMA films sandwiched by z-cut and fused quartz windows. (d) Thickness dependence of transmittance of IR at 2950 $cm^{-1}$.

clearly exhibits fringe patterns along the vertical axis at each specific wavenumber. Panel (b) of Fig. 3 shows an interferogram for sample 2, which underwent annealing at 433 K for 24 h. Although similar fringe patterns to those for sample 1 are observed, their periods are not identical. This discrepancy arises because the interferogram includes phase information generated from PMMA segments at the z-cut quartz substrate.

The phase for functional groups of PMMA at the quartz interface ($\phi_s$) can be extracted based on the interferograms for samples 1 and 2, as detailed in the supplementary material. In short, $\phi_S$ was given by the difference between the phases for samples 1 and 2. Eventually, since $|\chi_{eff}^{(2)}|$ is proportional to the square-root of the SFG intensity $\sqrt{I^{SFG}}$, $\mathrm{Re}\,\chi_{eff}^{(2)}$, and $\mathrm{Im}\,\chi_{eff}^{(2)}$ were obtained using $\cos\phi_S$, $\sin\phi_S$, and $\sqrt{I^{SFG}}$ for sample 2 based on Eq. (1). Panel (c) of Fig. 3 shows $\mathrm{Im}\,\chi_{eff}^{(2)}$ spectra for the 1- and 44 $\mu$m-thick well-annealed PMMA films. The ordinate was normalized by the value at 2950 $cm^{-1}$. Both spectra exhibited peaks at 2908 and 2950 $cm^{-1}$, corresponding to $CH_2$s and $OCH_3$s, respectively.[89] In addition, signals from $CH_2$as appeared as a shoulder at 2936 $cm^{-1}$. Although the shape of the spectra for the 1 $\mu$m-thick sample was almost identical to that of the 44 $\mu$m-thick one, the sign of the $\mathrm{Im}\,\chi_{eff}^{(2)}$ was opposite. This may be due to the difference in the contribution of the upper and lower interfaces to the SFG signals.

Taking into account that there are two interfaces, Int-1 and Int-2, as shown in the inset of Fig. 3(d), we now discuss which interface dominantly contributes to the $\mathrm{Im}\,\chi_{eff}^{(2)}$ spectra on the basis of the Fresnel coefficients at the interfaces.[92] At first, we examine the influence of beam absorption on the sample. The main panel of Fig. 3(d) shows the IR transmittance ($T$) through a PMMA film at a wavenumber of 2950 $cm^{-1}$ as a function of film thickness ($t$). The $T$ value simply decreased with increasing $t$ and was well reproduced by the Lambert–Beer law, as drawn by a solid curve. The $\varepsilon$ value at 2950 $cm^{-1}$ for the PMMA film was 2.2 × $10^3$ $cm^{-1}$. On the other hand, the $T$ value of the visible light with a wavelength of 532 nm passing through the PMMA film remained constant at unity. Taking into account the $T$ value of the input IR beam, the $\chi_{eff}^{(2)}$ value was obtained from Eq. (S16) in the supplementary material. Figure S2 summarizes the Fresnel coefficients at Int-1 and Int-2 as a function of thickness. While the Fresnel coefficient at Int-1 remained almost unchanged at (0.98 ± 0.08) with increasing $t$, that for Int-2 decreased, reaching 0 at around $d$ = 20 $\mu$m. In other words, in the case of the ~1 $\mu$m-thick film, the SFG signals generated from Int-1 could interfere with those from Int-2. Conversely, the SFG signals obtained from the 44 $\mu$m-thick film were only generated from Int-1. This situation was more suitable for analyzing the absolute interfacial orientation of functional groups than the 1 $\mu$m-thick one. Therefore, the 44 $\mu$m-thick film is adopted in the following analysis.

The absolute local conformation of PMMA chains at the quartz interface in the 44 $\mu$m-thick film after thermal annealing is discussed. All ps-SFG peaks shown in Fig. 3(c) were negative. Since the signal intensity from $OCH_3$s was the strongest, $\theta_{OCH_3}$ at Int-1 is here considered. The relationship between $\mathrm{Im}\,\chi_{eff}^{(2)}$ and $\theta_{OCH_3}$ is given by[93]

$$\mathrm{Im}\,\chi_{eff}^{(2)} \propto \frac{N\beta_{ccc}}{2}\left\{\langle\cos\theta_{OCH_3}\rangle(1+r) - \langle\cos\theta_{OCH_3}\rangle^3(1-r)\right\}, \quad (2)$$

where $N$ represents the number density of $OCH_3$ groups and $\beta_{ijk}$ is the microscopic hyperpolarizability tensor elements in the molecular coordinate system defined by the $a$, $b$, and $c$ axes.[89] In this case, the $\beta_{ccc}$ and $\beta_{aac}$ are the non-vanishing independent elements for the $OCH_3$s mode. Taking into account $r = \beta_{aac}/\beta_{ccc}$ = 1.8 and $\beta_{ccc}$ = −7.0,[89,93,94] negative $OCH_3$s signals can be satisfied with $\cos\theta > 0$. Therefore, the result indicates that the average orientation of $OCH_3$ groups pointed toward the z-axis.

The local conformation of PMMA chains at the quartz interface is also discussed based on the MD simulation. First, the analytical depth for the conventional and ps-SFG measurements was practically determined by comparing the MD results. Panel (a) of Fig. 4 shows a typical snap-shot of the model used in the MD simulation, which included both upper and lower interfaces. To obtain statistically meaningful data, the $\theta_{OCH_3}$ values near both interfaces were collected. Similar to the analysis of the ps-SFG measurements, the $\theta_{OCH_3}$ near the upper interface was defined as the angle between the O–C bond vector and the normal to the upper interface. On the other hand, the $\theta_{OCH_3}$ near the lower interface was the angle between such a bond vector and the normal to the lower interface.

The distribution of $\theta_{OCH_3}$ at a given depth region ($d$) was extracted from the MD simulation and is shown in Figs. 4(b) and S3 in the selected depth regions. Here, the subscript number for $d$ denotes the corresponding depth region. The number of $OCH_3$ groups that are oriented within the range from $\theta_{OCH_3}$ to $\theta_{OCH_3} + \Delta\theta$ is defined as $n(\theta_{OCH_3})$. In the case of the isotropic orientation of $OCH_3$ groups, the distribution of $\theta_{OCH_3}$ can be expressed by a sine function as below:

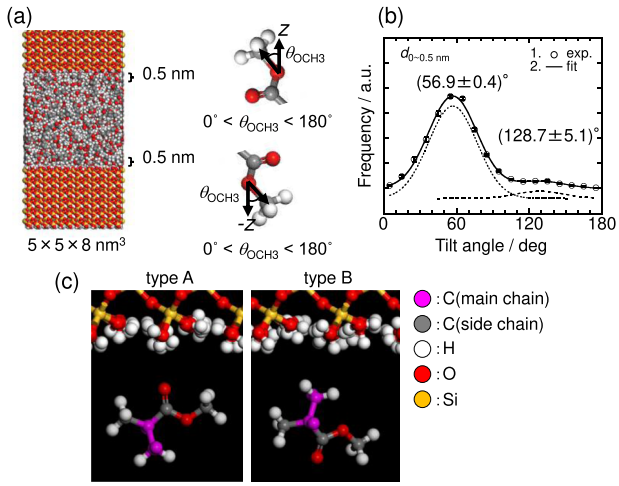


**FIG. 4.** (a) A simulation model of the PMMA interface with the quartz surface. Atoms are drawn by a space-filling molecular model. The tilt angle for $OCH_3$ groups ($\theta_{OCH_3}$) is defined. (b) Tilt angle distribution for $OCH_3$ groups in the depth region from 0 to 0.5 nm from the quartz surface. Open circles are data. Broken and solid curves are the best fit to two peaks and the sum of them, respectively. The standard deviation expressed by an error bar is less than 0.2%. (c) Representative local conformations of a PMMA segment. Molecules are drawn by a ball-stick model in which chemical bonds are emphasized in comparison with atoms in size. Purple balls and sticks represent the atoms and bonds of the backbone.

$$\frac{n(\theta_{OCH_3})}{N_{sr}}\Delta\theta = \frac{2\pi {r_a}^2 \sin\theta_{OCH_3}}{4\pi {r_a}^2}\Delta\theta = \frac{1}{2}\sin\theta_{OCH_3}\Delta\theta, \quad (3)$$

where $N_{sr}$ and $r_a$ are the total number of $OCH_3$ groups in the spherical region and the radius of the sphere, respectively. In the case of $d_{2.0-2.5\,nm}$ [Fig. S3(d)], the histogram was expressed by a sine function, implying that the orientation of $OCH_3$ groups was isotropic. This trend was also discerned for $d_{1.0-1.5\,nm}$ and $d_{1.5-2.0\,nm}$, as shown in Figs. S3(b) and S3(c). However, in the case of $d_{0.5-1.0\,nm}$, the $\theta_{OCH_3}$ distribution deviated from a sine curve. This became more remarkable in a shallower depth region, i.e., in the case of $d_{0-0.5\,nm}$, as shown in Fig. 4(b). Considering that the orientation of $OCH_3$ groups was observed in the SFG spectrum shown in Fig. 2, it seems reasonable to claim that the analytical depth of SFG for this system could be less than 1 nm.

Panel (b) of Fig. 4 shows a distribution of $\theta_{OCH_3}$ at $d_{0-0.5\,nm}$ obtained from the MD simulation at 298 K for 1 ns. Two Gaussian functions were used to fit the data. The analysis revealed a major peak centered at $\theta_{OCH_3}$ of $(56.9 \pm 0.4)^\circ$ with a full width at half maximum (FWHM) of $(47.0 \pm 1.0)^\circ$, along with a minor peak at $\theta_{OCH_3}$ of $(128.7 \pm 5.1)^\circ$ with a FWHM of $(47.5 \pm 12.9)^\circ$. Hence, it is reasonable to propose the existence of two distinct local conformations, referred to as types A and B, each exhibiting a certain angular distribution. In addition, the $\theta_{OCH_3}$ value for the major component of type A was in good agreement with that obtained from the conventional SFG measurements ($= 63^\circ$).

Panel (c) of Fig. 4 shows representative local conformations of types A and B. To depict these conformations, the upper interface was selected, as the SFG signals were primarily generated from Int-1. In the type A conformation, C=O groups are oriented toward the quartz interface. Conversely, in the type B conformation, ether oxygen atoms are most likely to interact with the quartz surface. The area ratio between type A and type B conformations was determined to be 92.7:7.3, indicating that the dominant component at the interface is the type A conformation. Additionally, while $CH_2$ groups in the type A conformation were found to migrate into the internal region, those in the type B conformation were observed to be oriented toward the SiOH interface. The conventional and ps-SFG spectra of the annealed film demonstrated that signals for $OCH_3$s were markedly stronger than those for $CH_2$s and $CH_2$as, as shown in Figs. 2 and 3(c). This indicates that $OCH_3$ groups were predominantly oriented at the interface. Consequently, the findings from the MD simulation align well with the results obtained from both conventional and ps-SFG measurements.

Finally, the energetically preferable conformation between type A and type B is discussed. To assess this, the total potential energy of a chain was calculated in two scenarios: when it existed in a vacuum and when it was adsorbed on the SiOH interface. The difference in total potential energy between these two states, referred to as the adsorption energy ($\Delta E_{ad}$), was determined. The $\Delta E_{ad}$ values for types A and B were found to be $-52.5$ and $-23.8$ kJ·mol$^{-1}$, respectively, indicating that the local conformation of type A was more energetically stable than type B. This preference can primarily be attributed to the hydrogen bonding between C=O groups and SiOH groups at the substrate surface.

## CONCLUSIONS

We examined the absolute local conformation of PMMA chains in direct contact with a quartz surface using conventional and ps-SFG measurements in conjunction with MD simulations. Conventional SFG showed that $CH_2$ groups of the main chain part and $OCH_3$ groups of the side chain at the interface re-oriented upon thermal annealing. The ps-SFG measurements further indicated that $OCH_3$ groups were predominantly oriented toward the quartz side after thermal annealing. In addition, by combining the results obtained from SFG spectroscopy and MD simulation, it was found that the inversion symmetry of the orientational distribution in the PMMA film was broken within the depth range of less than 1 nm from the interface with quartz. Further analysis revealed that in this depth region, many of the carbonyl groups and some ether groups interacted with OH groups on the quartz surface. This interaction was attributed to the larger adsorption energy resulting from the formation of hydrogen bonding for the former compared to the latter. These findings are crucial for gaining a better understanding of the complex aggregation states of polymer chains at buried interfaces with fillers or substrates.

## SUPPLEMENTARY MATERIAL

Calculations of the phase of SFG signals, the tilt angle of $OCH_3$ groups and Fresnel coefficients, and the effective tilt angle distribution were extracted from the MD simulation as a function of depth.

## ACKNOWLEDGMENTS

This work was partly supported by JSPS KAKENHI Grant-in-Aids for Scientific Research (B) (Grant No. JP20H02790) to K.T. and for Scientific Research (B) (Grant No. JP20H02802) to D.K. from the Ministry of Education, Culture, Sports, Science and Technology (MEXT), Japan. We also acknowledge the support from the JST-Mirai Program (Grant No. JPMJMI18A2) (K.T.).

## AUTHOR DECLARATIONS

### Conflict of Interest

The authors have no conflicts to disclose.

### Author Contributions

**Daisuke Kawaguchi**: Data curation (equal); Formal analysis (lead); Funding acquisition (supporting); Investigation (equal); Methodology (equal); Validation (equal); Writing – original draft (lead). **Kazuki Sasahara**: Formal analysis (lead); Investigation (lead); Methodology (equal); Validation (equal); Writing – original draft (equal). **Manabu Inutsuka**: Formal analysis (supporting); Investigation (supporting); Validation (equal). **Tatsuki Abe**: Formal analysis (supporting); Investigation (supporting); Validation (equal); Writing – original draft (supporting). **Satoru Yamamoto**: Formal analysis (supporting); Investigation (supporting); Validation (equal);

Writing – original draft (supporting). **Keiji Tanaka**: Conceptualization (lead); Data curation (equal); Funding acquisition (lead); Investigation (equal); Methodology (equal); Supervision (lead); Validation (equal); Writing – review & editing (lead).

## DATA AVAILABILITY

The data that support the findings of this study are available from the corresponding authors upon reasonable request.

## REFERENCES


[1] A. Bansal, H. C. Yang, C. Z. Li, K. W. Cho, B. C. Benicewicz, S. K. Kumar, and L. S. Schadler, Nat. Mater. **4**, 693 (2005).
[2] L. S. Schadler, S. K. Kumar, B. C. Benicewicz, S. L. Lewis, and S. E. Harton, MRS Bull. **32**, 335 (2007).
[3] H. Oh and P. F. Green, Nat. Mater. **8**, 139 (2009).
[4] M. J. A. Hore and R. J. Composto, Macromolecules **45**, 6078 (2012).
[5] J. James, A. B. Unni, K. Taleb, J.-P. Chapel, N. Kalarikkal, S. Varghese, G. Vignaud, and Y. Grohens, Nano-Struct. Nano-Objects **17**, 34 (2019).
[6] M. J. A. Hore, Soft Matter **15**, 1120 (2019).
[7] E. J. Bailey and K. I. Winey, Prog. Polym. Sci. **105**, 101242 (2020).
[8] M. J. A. Hore, in *Theory and Modeling of Polymer Nanocomposites*, edited by V. V. Ginzburg and L. M. Hall (Springer International Publishing, Cham, 2021), p. 259.
[9] T. Kimura and M. Hayashi, Polym. J. **54**, 1307 (2022).
[10] A. Yamaguchi, M. Urushisaki, H. Uematsu, T. Sakaguchi, and T. Hashimoto, Polym. J. **55**, 153 (2023).
[11] Y. Qiang, K. T. Turner, and D. Lee, Macromolecules **56**, 122 (2023).
[12] S. E. Root, S. Savagatrup, A. D. Printz, D. Rodriquez, and D. J. Lipomi, Chem. Rev. **117**, 6467 (2017).
[13] X. Wang, S. Meng, W. Ma, J. Pionteck, M. Gnanaseelan, Z. Zhou, B. Sun, Z. Qin, and M. Zhu, React. Funct. Polym. **112**, 74 (2017).
[14] K. Bagchi, C. Deng, C. Bishop, Y. Li, N. E. Jackson, L. Yu, M. F. Toney, J. J. de Pablo, and M. D. Ediger, ACS Appl. Mater. Interfaces **12**, 26717 (2020).
[15] M. Ashizawa, Y. Zheng, H. Tran, and Z. Bao, Prog. Polym. Sci. **100**, 101181 (2020).
[16] T. J. Ferron, J. L. Thelen, K. Bagchi, C. Deng, E. Gann, J. J. de Pablo, M. D. Ediger, D. F. Sunday, and D. M. DeLongchamp, ACS Appl. Mater. Interfaces **14**, 3455 (2022).
[17] P. Das and B. C. Thompson, Polym. J. **55**, 317 (2023).
[18] D. Kawaguchi, A. Higasayama, Y. Ogata, T. Kabe, Y. Matsushita, and K. Tanaka, Polym. J. **55**, 497 (2023).
[19] R. A. L. Jones, Curr. Opin. Solid State Mater. Sci. **2**, 673 (1997).
[20] J. Duchet, J.-P. Chapel, B. Chabert, and J.-F. Gerard, Macromolecules **31**, 8264 (1998).
[21] S. Y. Fu, X. Q. Feng, B. Lauke, and Y. W. Mai, Composites, Part B **39**, 933 (2008).
[22] K. Yamaguchi, D. Kawaguchi, N. Miyata, T. Miyazaki, H. Aoki, S. Yamamoto, and K. Tanaka, Phys. Chem. Chem. Phys. **24**, 21578 (2022).
[23] S. Inata, H. Sogawa, and F. Sanda, Polym. J. **55**, 785 (2023).
[24] D. Rossi, Y. Wu, R. Paradkar, Y. Dong, X. Chen, C. J. Tucker, C. Mohler, T.-C. Kuo, and Z. Chen, Ind. Eng. Chem. Res. **62**, 13880 (2023).
[25] T. Nishi, J. Polym. Sci., Polym. Phys. Ed. **12**, 685 (1974).
[26] B. Meissner, J. Appl. Polym. Sci. **50**, 285 (1993).
[27] G. Heinrich, M. Klüppel, and T. A. Vilgis, Curr. Opin. Solid State Mater. Sci. **6**, 195 (2002).
[28] Y. Fujii, Z. H. Yang, J. Leach, H. Atarashi, K. Tanaka, and O. K. C. Tsui, Macromolecules **42**, 7418 (2009).
[29] S. Napolitano and M. Wübbenhorst, Nat. Commun. **2**, 260 (2011).
[30] P. Gin, N. Jiang, C. Liang, T. Taniguchi, B. Akgun, S. K. Satija, M. K. Endoh, and T. Koga, Phys. Rev. Lett. **109**, 265501 (2012).
[31] S. Sun, H. Xu, J. Han, Y. Zhu, B. Zuo, X. Wang, and W. Zhang, Soft Matter **12**, 8348 (2016).
[32] D. A. Barkley, N. Jiang, M. Sen, M. K. Endoh, J. G. Rudick, T. Koga, Y. Zhang, O. Gang, G. Yuan, S. K. Satija, D. Kawaguchi, K. Tanaka, and A. Karim, Macromolecules **50**, 7657 (2017).
[33] Y. Hong, S. Bao, X. Xiang, and X. Wang, ACS Macro Lett. **9**, 889 (2020).
[34] K. Paeng, R. Richert, and M. D. Ediger, Soft Matter **8**, 819 (2012).
[35] H. K. Nguyen, S. Sugimoto, A. Konomi, M. Inutsuka, D. Kawaguchi, and K. Tanaka, ACS Macro Lett. **8**, 1006 (2019).
[36] M. A. Sattar and A. Patnaik, ACS Omega **5**, 21191 (2020).
[37] V. A. Bershtein, O. P. Grigoryeva, P. N. Yakushev, and A. M. Fainleib, Polym. Compos. **42**, 6777 (2021).
[38] T. Rahman and D. S. Simmons, Macromolecules **54**, 5935 (2021).
[39] Z. Hao, A. Ghanekarade, N. Zhu, K. Randazzo, D. Kawaguchi, K. Tanaka, X. Wang, D. S. Simmons, R. D. Priestley, and B. Zuo, Nature **596**, 372 (2021).
[40] C. B. Roth, Chem. Soc. Rev. **50**, 8050 (2021).
[41] R. B. Venkatesh and D. Lee, Macromolecules **55**, 4492 (2022).
[42] J. H. Merrill, R. Li, and C. B. Roth, ACS Macro Lett. **12**, 1 (2023).
[43] W. Ren, Y. Hong, H. Wei, J. Xu, C. Zhang, X. Zhou, and X. Wang, Macromolecules **56**, 1410 (2023).
[44] Z. Huang, Y. Bajaj, J.-M. Y. Carrillo, Y. Nakanishi, K. Uchida, K. Mita, T. Yamada, T. Miyazaki, B. G. Sumpter, M. Endoh, and T. Koga, Polymer **265**, 125584 (2023).
[45] T. Miyazaki, N. Miyata, M. Asada, Y. Tsumura, N. Torikai, H. Aoki, K. Yamamoto, T. Kanaya, D. Kawaguchi, and K. Tanaka, Langmuir **35**, 11099 (2019).
[46] K. S. Schweizer and D. S. Simmons, J. Chem. Phys. **151**, 240901 (2019).
[47] M. F. Thees, J. A. McGuire, and C. B. Roth, Soft Matter **16**, 5366 (2020).
[48] S. Napolitano, Soft Matter **16**, 5348 (2020).
[49] J. Giermanska, S. Ben Jabrallah, N. Delorme, G. Vignaud, and J.-P. Chapel, Polymer **228**, 123934 (2021).
[50] S. Sugimoto, M. Inutsuka, D. Kawaguchi, and K. Tanaka, Polym. J. **52**, 217 (2020).
[51] J. Champagne, S. Cantournet, D. Colombo, S. Jamonneau, K. Le Gorju, F. Lequeux, and H. Montes, Macromolecules **53**, 3728 (2020).
[52] D. Salatto, J.-M. Y. Carrillo, M. K. Endoh, T. Taniguchi, B. M. Yavitt, T. Masui, H. Kishimoto, M. Tyagi, A. E. Ribbe, V. Garcia Sakai, M. Kruteva, B. G. Sumpter, B. Farago, D. Richter, M. Nagao, and T. Koga, Macromolecules **54**, 11032 (2021).
[53] W. Ren, X. Wang, J. Shi, J. Xu, H. Taneda, N. L. Yamada, D. Kawaguchi, K. Tanaka, and X. Wang, Soft Matter **18**, 1997 (2022).
[54] M. Inutsuka, H. Watanabe, M. Aoyagi, N. L. Yamada, C. Tanaka, T. Ikehara, D. Kawaguchi, S. Yamamoto, and K. Tanaka, ACS Macro Lett. **11**, 504 (2022).
[55] Y. Qiang, S. S. Pande, D. Lee, and K. T. Turner, ACS Nano **16**, 6372 (2022).
[56] C. A. J. Hoeve, E. A. DiMarzio, and P. Peyser, J. Chem. Phys. **42**, 2558 (1965).
[57] J. M. H. M. Scheutjens and G. J. Fleer, J. Phys. Chem. **84**, 178 (1980).
[58] Y. Oda, D. Kawaguchi, Y. Morimitsu, S. Yamamoto, and K. Tanaka, Sci. Rep. **10**, 20914 (2020).
[59] Y. Morimitsu, H. Matsuno, Y. Oda, S. Yamamoto, and K. Tanaka, Sci. Adv. **8**, eabn6349 (2022).
[60] Y. R. Shen, Nature **337**, 519 (1989).
[61] Z. Chen, Y. R. Shen, and G. A. Somorjai, Annu. Rev. Phys. Chem. **53**, 437 (2002).
[62] A. Horinouchi, H. Atarashi, Y. Fujii, and K. Tanaka, Macromolecules **45**, 4638 (2012).
[63] Y. Oda, A. Horinouchi, D. Kawaguchi, H. Matsuno, S. Kanaoka, S. Aoshima, and K. Tanaka, Langmuir **30**, 1215 (2014).
[64] M. Inutsuka, A. Horinouchi, and K. Tanaka, ACS Macro Lett. **4**, 1174 (2015).
[65] H. K. Nguyen, M. Inutsuka, D. Kawaguchi, and K. Tanaka, J. Chem. Phys. **146**, 203313 (2017).
[66] S. Sugimoto, M. Inutsuka, D. Kawaguchi, and K. Tanaka, ACS Macro Lett. **7**, 85 (2018).
[67] B. Zuo, M. Inutsuka, D. Kawaguchi, X. P. Wang, and K. Tanaka, Macromolecules **51**, 2180 (2018).

[68]D. Kawaguchi, K. Yamamoto, T. Abe, N. Jiang, T. Koga, S. Yamamoto, and K. Tanaka, Phys. Chem. Chem. Phys. **23**, 23466 (2021).
[69]R. Harada, D. Kawaguchi, S. Yamamoto, and K. Tanaka, Soft Matter **18**, 3304 (2022).
[70]T. Abe, H. Shimada, T. Hoshino, D. Kawaguchi, and K. Tanaka, Polym. J. **54**, 679 (2022).
[71]N. Ji, V. Ostroverkhov, C. Y. Chen, and Y. R. Shen, J. Am. Chem. Soc. **129**, 10056 (2007).
[72]N. Ji, V. Ostroverkhov, C. S. Tian, and Y. R. Shen, Phys. Rev. Lett. **100**, 096102 (2008).
[73]S. Yamaguchi and T. Tahara, J. Chem. Phys. **129**, 101102 (2008).
[74]Y. R. Shen, Annu. Rev. Phys. Chem. **64**, 129 (2013).
[75]C. S. Tian and Y. R. Shen, Surf. Sci. Rep. **69**, 105 (2014).
[76]H. Watanabe, S. Yamaguchi, S. Sen, A. Morita, and T. Tahara, J. Chem. Phys. **132**, 144701 (2010).
[77]W. Hua, D. Verreault, Z. Huang, E. M. Adams, and H. C. Allen, J. Phys. Chem. B **118**, 8433 (2014).
[78]D. Hu and K. C. Chou, J. Am. Chem. Soc. **136**, 15114 (2014).
[79]M. J. Hofmann and P. Koelsch, J. Chem. Phys. **143**, 134112 (2015).
[80]N. Takeshita, M. Okuno, and T.-A. Ishibashi, Phys. Chem. Chem. Phys. **19**, 2060 (2017).
[81]X. F. Han, C. Leng, Q. Shao, S. Y. Jiang, and Z. Chen, Langmuir **35**, 1327 (2019).
[82]E. Tyrode, C. M. Johnson, M. W. Rutland, and P. M. Claesson, J. Phys. Chem. C **111**, 11642 (2007).
[83]W.-C. Yang and D. K. Hore, J. Phys. Chem. C **121**, 28043 (2017).
[84]M. Okuno, O. Homma, A. T. Kuo, S. Urata, R. Koguchi, T. Miyajima, and T. Ishibashi, Macromolecules **52**, 8705 (2019).
[85]A. Myalitsin, S. Ghosh, S. Urashima, S. Nihonyanagi, S. Yamaguchi, T. Aoki, and T. Tahara, Phys. Chem. Chem. Phys. **22**, 16527 (2020).
[86]B. Li, L. Chen, S. Zhang, Q. Tao, Y.-H. Ma, P. Hu, X. Lu, K. C. Chou, and Z. Chen, Appl. Surf. Sci. **611**, 155715 (2023).
[87]H. Vogel, Phys. Z. **22**, 645 (1921).
[88]C. L. Brooks III, B. M. Pettitt, and M. Karplus, J. Chem. Phys. **83**, 5897 (1985).
[89]Y. Tateishi, N. Kai, H. Noguchi, K. Uosaki, T. Nagamura, and K. Tanaka, Polym. Chem. **1**, 303 (2010).
[90]Y. M. Hong, H. Zhou, W. H. Qian, B. Zuo, and X. P. Wang, J. Phys. Chem. C **121**, 19816 (2017).
[91]C. Hirose, N. Akamatsu, and K. Domen, J. Chem. Phys. **96**, 997 (1992).
[92]X. Lu, N. Shephard, J. Han, G. Xue, and Z. Chen, Macromolecules **41**, 8770 (2008).
[93]H. Zhu, K. C. Jha, R. S. Bhatta, M. Tsige, and A. Dhinojwala, Langmuir **30**, 11609 (2014).
[94]J. Wang, C. Y. Chen, S. M. Buck, and Z. Chen, J. Phys. Chem. B **105**, 12118 (2001).